Polysynthetic Twinning in RbIn$_3$S$_5$

L. Kienle[1] and A. Simon

Max Planck Institut für Festkörperforschung, Heisenbergstr. 1, 70569 Stuttgart, Germany

The real structure of the new ternary compound **RbIn$_3$S$_5$** is characterized by polysynthetic twinning of nanosized domains separated by coherent twin boundaries. Based on electron microscopy, a model of the structure at the twin interface is derived which allows a convincing simulation of experimental images. The details of twinning are described in a unified model. As a rule, a disordered arrangement of twin lamellas with a random distribution of their widths is observed with ordering of twin boundaries only in nanosized regions of the crystallites. For a minimal distance of the twin boundaries (back-to-back twinning) the close relationship between twinning and shearing is discussed. The distinction of these two cases is only possible by close inspection of the atomic structure at the boundaries. Twinning is not the only crystal defect in the structure of RbIn$_3$S$_5$. Variations in the connection of the characteristic structural units occur which lead to the formation of different real structures. © 2002 Elsevier Science (USA)

Key Words: high-resolution electron microscopy; twinning; Image simulation; crystal defects.

INTRODUCTION

Ternary indium chalcogenides of monovalent metals play an important role in application-orientated research. In particular, several semiconducting materials in the system Cu–In–Se have intensively been examined due to their promising quality in the conversion of solar energy (1). Many of these compounds [e.g., CuInSe$_2$ (2,3), CuIn$_5$Se$_8$ (4,5) and CuIn$_3$Se$_5$ (6,7)] are characterized by complex defect structures. Hence, electron microscopy is an important tool for the understanding of their real structures. In contrast to the frequently examined copper compounds, ternary alkali metal indium chalcogenides have been only rarely analyzed (8,9). In the case of the ternary system M–In–S (M = K, Rb, Cs) the coexistence of many compounds with slightly different compositions and complex structures has been established [e.g., KIn$_5$S$_6$ (10),

KIn$_5$S$_7$ (10) and KIn$_5$S$_8$ (11)].The syntheses of homogeneous samples of new compounds are troublesome without the exact knowledge of the yet unknown composition. For M = Rb and Cs, first attempts to prepare new compounds resulted in heterogeneous samples which cannot be analyzed easily by standard XRD methods. The transmission electron microscope offers the possibility to determine simultaneously the composition by energy dispersive X-ray spectroscopy (EDXS) and to identify the different components by electron diffraction (9). When analyzing different samples with nominal compositions MIn$_7$S$_9$ (M = Rb, Cs), we came to the conclusion that new compounds with an approximate composition of MIn$_3$S$_5$ were present besides MInS$_2$ and MIn$_7$S$_9$. On the basis of these observations several grams of pure MIn$_3$S$_5$ could be prepared starting from the elements.

X-ray diffraction (XRD) investigations (12) on several single crystals of the Rb and Cs containing compounds led to a structure model characterized by remarkable crystallographic anomalies which were particularly obvious for M = Rb (i.e., high residual density, wR_2 > 25%). Hence, this compound was chosen to investigate into these anomalies. High residual densities (up to $30\,\text{e}/\text{Å}^3$) imply that this model contains artifacts. An idealized structure (in the following called "ideal structure," see Table 1) neglects all anomalies and serves as a basis for the discussion of the real structure of RbIn$_3$S$_5$. Simulations of XRD powder patterns based on this ideal model are in good agreement with experimental ones. Thus crystal defects could be responsible for the observed anomalies of the single crystal data, in particular, as the crystal faces are clearly striped.

According to the ideal structure model (spacegroup: $P2/m$) RbIn$_3$S$_5$ is characterized by a complex framework of sulfur atoms and two different coordination spheres for both cations (Rb$^+$ and In^{3+}) by S^{2-}.[2] The corresponding coordination polyhedra can be regarded as building units of the structure. The coordination numbers (CN) for Rb$^+$ are 10 and 9, the respective polyhedra will be designated as

---

[1] To whom correspondence should be addressed. Fax: +49-07116891091. E-mail: lkienle@sim.mpi-stuttgart.mpg.de.

[2] The structure can also be described as ccp array of S^{2-} and Rb$^+$ (see (12)).

TABLE 1
Atomic Coordinates for the Ideal Structure of RbIn$_3$S$_5$ (SpaceGroup: $P2/m$, $a = 12.393$ Å, $b = 3.777$ Å, $c = 15.385$ Å, $\beta = 112.6°$

Atom	Site	x	y	z
In1	2n	0.17463	$\frac{1}{2}$	0.16434
In2	1h	$\frac{1}{2}$	$\frac{1}{2}$	$\frac{1}{2}$
In3	2m	0.47711	0	0.28617
In4	2n	0.77068	$\frac{1}{2}$	0.26912
In5	2m	0.88273	0	0.07116
S1	2m	0.26799	0	0.10184
S2	2n	0.55614	$\frac{1}{2}$	0.21401
S3	2m	1.06529	0	0.21474
S4	2m	0.61215	0	0.45482
S5	2n	0.77066	$\frac{1}{2}$	0.10827
S6	2m	0.86556	0	0.36484
S7	2n	0.35308	$\frac{1}{2}$	0.32046
S8	1b	0	$\frac{1}{2}$	0
Rb1	1d	$\frac{1}{2}$	0	0
Rb2	2n	0.13386	$\frac{1}{2}$	0.42747

"single polyhedron" and "condensed polyhedron". The single polyhedron exhibits only small deviations from an orthorhombic symmetry (see Fig. 1a), and therefore it can be described as bicapped orthorhombic prism. The condensed polyhedron consists of two distorted singly capped prisms sharing one common face (see Fig. 1b). Both types of polyhedra are connected via common faces to
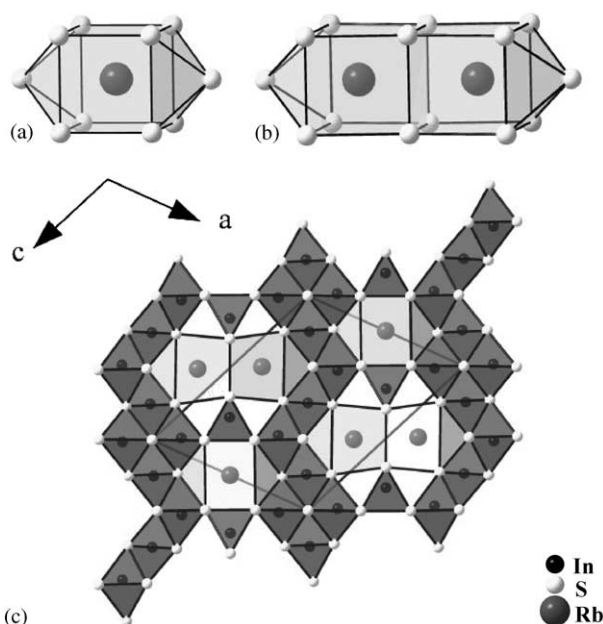

FIG. 1. Coordination polyhedra in RbIn$_3$S$_5$ and their connection: (a) single polyhedron, (b) condensed polyhedron centered by Rb$^+$; (c) projection of the structure in polyhedral representation (light gray: single and condensed polyhedra centered by Rb$^+$, dark gray: octahedra and tetrahedra centered by In^{3+}).

form columns along [010]. InS$_4$ tetrahedra and InS$_6$ octahedra connect these columns perpendicular to [010] as one can see in the polyhedral representation in Fig. 1c (projection along [010]). The InS$_4$ tetrahedra share common corners forming "Einer-Einfachketten" [according to (13)] along [010]. Layers of corner- and edge-sharing InS$_6$ octahedra (viewed edge-on in Fig. 1c) are completing the ideal structure of RbIn$_3$S$_5$.

EXPERIMENTAL

Selected crystals of RbIn$_3$S$_5$ were crushed in an agate mortar and suspended in *n*-butanol. A perforated carbon/copper net was covered with the suspension, leaving wedge-shaped crystallites in random orientations after drying. These nets were fixed in a side-entry, double-tilt holder with the tilting limited to a maximum of $\pm 25°$ in two directions. High-resolution electron microscopy (HREM) and selected-area electron diffraction (SAED) were performed in a Philips CM30/ST using an LaB$_6$ cathode. Operating at 300 kV the point resolution is 1.9 Å, the value of the Scherzer defocus optimum is -58 nm. Computer simulations of kinematical electron diffraction patterns and HREM images (multislice formalism) were calculated with the EMS program package [(14), basic parameters for the image simulation: spherical aberration constant $C_S = 1.15$ mm, defocus spread $\Delta = 7$ nm, illumination semi-angle $\alpha = 1.2$ mrad]. HREM images and SAED patterns were registered with a slow-scan CCD camera (Gatan, 1024×1024 pixels, pixel size: 24×24 μm^2). The software "Digital Micrograph 2.5" (Gatan) was used for processing the high-resolution images. In order to reduce the small amount of noise resulting from an amorphous surface layer on the crystals, all HREM images were filtered after Fourier transformation by using a suitable band-pass mask. Great care was taken to avoid loss of essential information of the defect structure by image processing. For a highlighted visualization of nanosized domains, a different procedure was applied which is explicitly described in the corresponding part of the text.

RESULTS

Structure of Defect-Free Crystals

Many of the crystallites were aligned with their zone axis [010] parallel to the electron beam. In a first step, the ideal structure model (see Table 1) resulting from XRD data was checked by HREM and SAED. The diffraction patterns of crystallites with no evident defects can be completely indexed assuming the ideal structure model. Figure 2a represents a series of HREM micrographs with inserted computer-simulated images based on the ideal structure model (different defocus values, zone axis [010]). The good
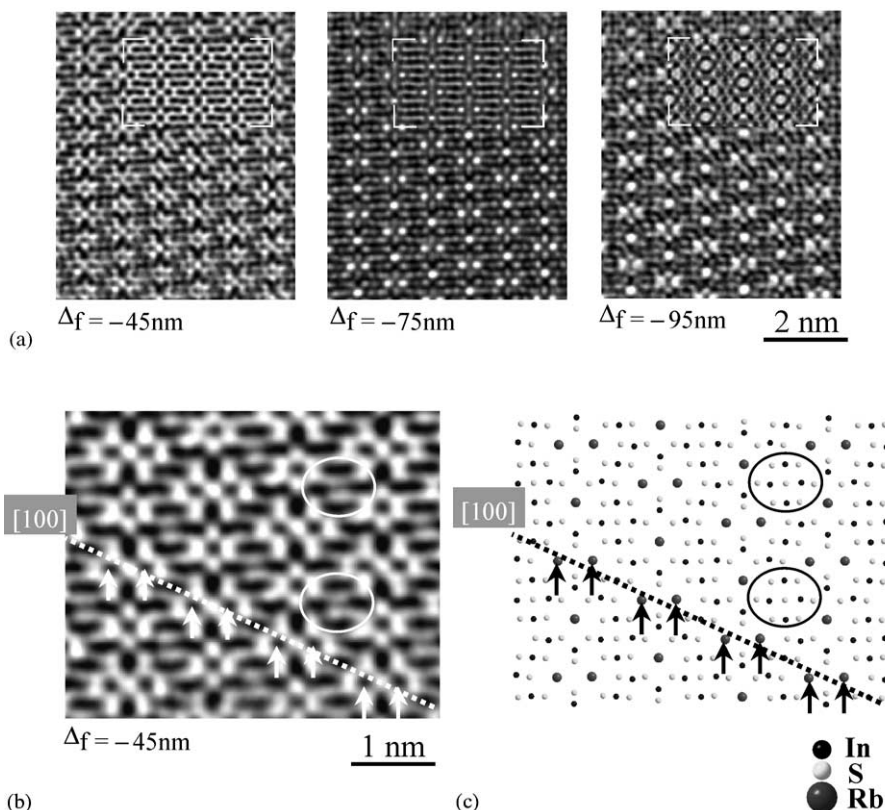
FIG. 2. (a) Series of HREM micrographs with variable defocus Δf and inserted simulated images (zone axis: [010], thickness: 3.8 nm), (b) HREM image taken near Scherzer defocus, (c) projection of the structure. For markings see text.

agreement between experimental and simulated images can also be observed for all other examined zone axes (including [001], [101] and [100]). This gives evidence for a correct description of the structure of these crystals by the ideal structure model. In particular, no unexpected contrasts were observed at positions with high residual densities in the XRD analysis (see above). Figure 2b represents an enlarged section of an image taken from a thin region of a wedge-shaped crystal near the Scherzer defocus optimum. Within the weak-phase approximation, the positions with a high value of the projected potential are represented by black features and the cavities of the structure (corresponding to low values of the projected potential) by white features. Hence, the projection of the ideal structure in Fig. 2c allows the direct interpretation of this image. The arrows mark pairs of clearly resolved dark spots (Fig. 2b) corresponding to the potential of the rubidium atoms centering the condensed polyhedra ($d_{\mathrm{Rb-Rb}} = 4.655\,\mathring{\mathrm{A}}$). These contrasts are connected by a dashed line parallel [100] in Figs. 2b and 2c. Due to the limited resolution of the microscope, most of the closely neighbored indium and sulfur atoms of the InS_6 octahedra

and InS_4 tetrahedra are not resolved in the images along [010]. Nevertheless, the periodical array of the contrasts is in agreement with the periodical arrangement of e.g., indium and sulfur atoms forming blocks of InS_6 octahedra indicated by ellipsoidal marks in Figs. 2b and 2c.

Characterization of the Twinning

A first indication for twinning appears in SAED experiments which allow to scan for the presence of real structure phenomena in aligned crystallites by shifting the position of the SAED diaphragm relative to the crystal surface. Occasionally, the sizes of the single domains are large enough to record their diffraction patterns sequentially. The different orientations of the twin domains are evident from Figs. 3a–3c. The SAED pattern of a single domain (Figs. 3a or 3c) changes dramatically when a second domain contributes to the electron diffraction pattern in the shifting experiment. The superimposed diffraction patterns of a twinned region (Fig. 3b) exhibit higher symmetry due to mirror planes perpendicular to [102]* and [$\bar{1}$01]*. Hence, an unambiguous derivation of
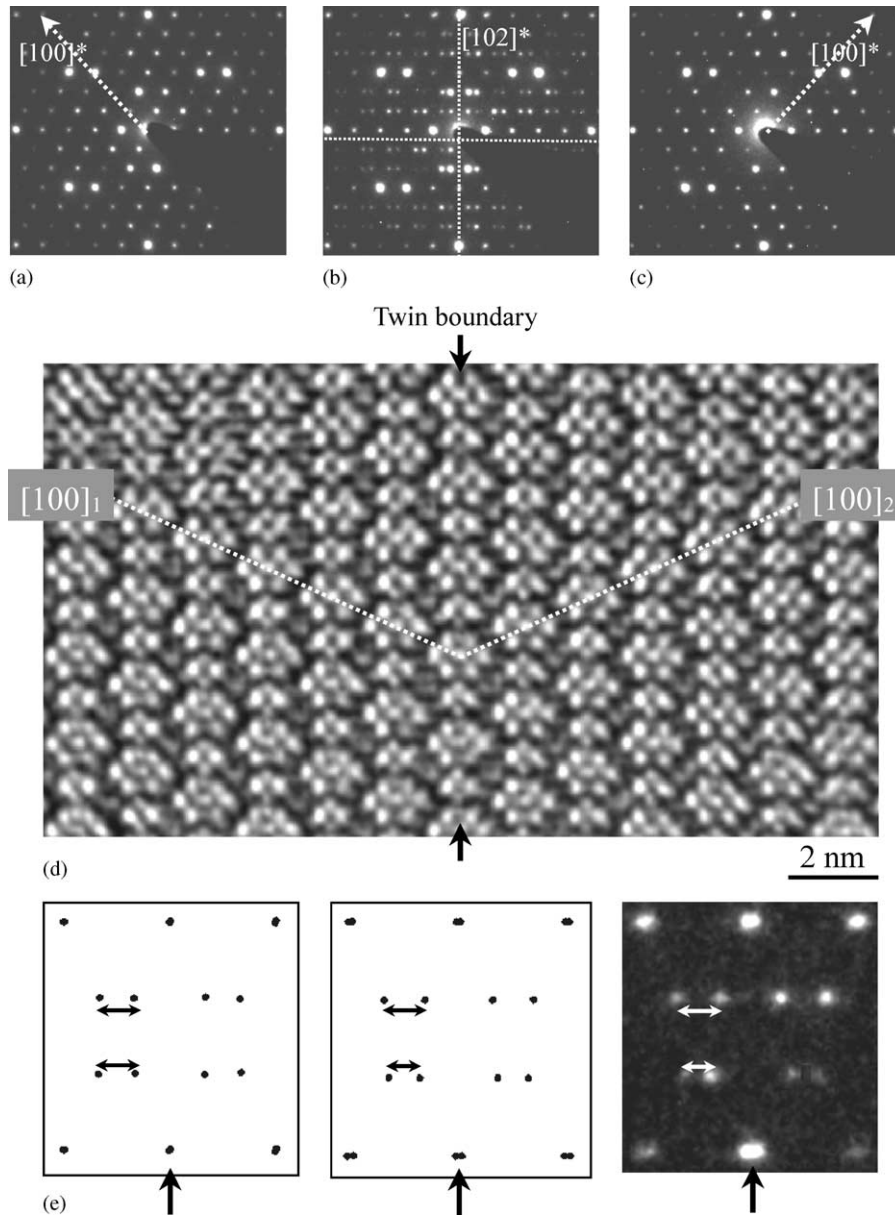
FIG. 3. (a)–(c) SAED patterns obtained on twinned crystals (zone axis [010]), shifting the position of the crystal relative to the position of the SAED diaphragm. (a) SAED pattern of the domain in orientation 1, (c) pattern of the domain in orientation 2 (the dashed arrows indicate [100]*), (b) pattern containing information on both domains (superposition). (d) HREM image displaying the twin boundary (the dashed lines indicate [100] for orientations 1 and 2). (e) Left and center: simulation of the geometry of SAED patterns varying the orientation of the twin element with respect to [20$\bar{1}$] (left: 89.7°, center: 90°), right: corresponding section of an experimental SAED pattern.

the twin law from diffraction experiments is not trivial. In order to find the real orientation of the twin element it is important to analyze the high resolution micrograph (Fig. 3d). It is evident that the boundary between the two twin domains (marked by the arrows in Fig. 3d) containing the twin element is orientated perpendicular to [20$\bar{1}$] which corresponds to [$\bar{1}$01]* in reciprocal space. The dashed lines in Fig. 3d run along [100] of the domains (index 1 or 2) and connect contrasts corresponding to the potential of the rubidium atoms in the centers of the condensed polyhedra. For comparison see the related line for a single domain in Fig. 2b. The reflection of these contrasts at the domain boundary is obvious.

The twinning can be described as twinning by reticular pseudo-merohedry (see Fig. 2b). At first glance, reflections $hkl, h + l = 3n$ coincide and reflections
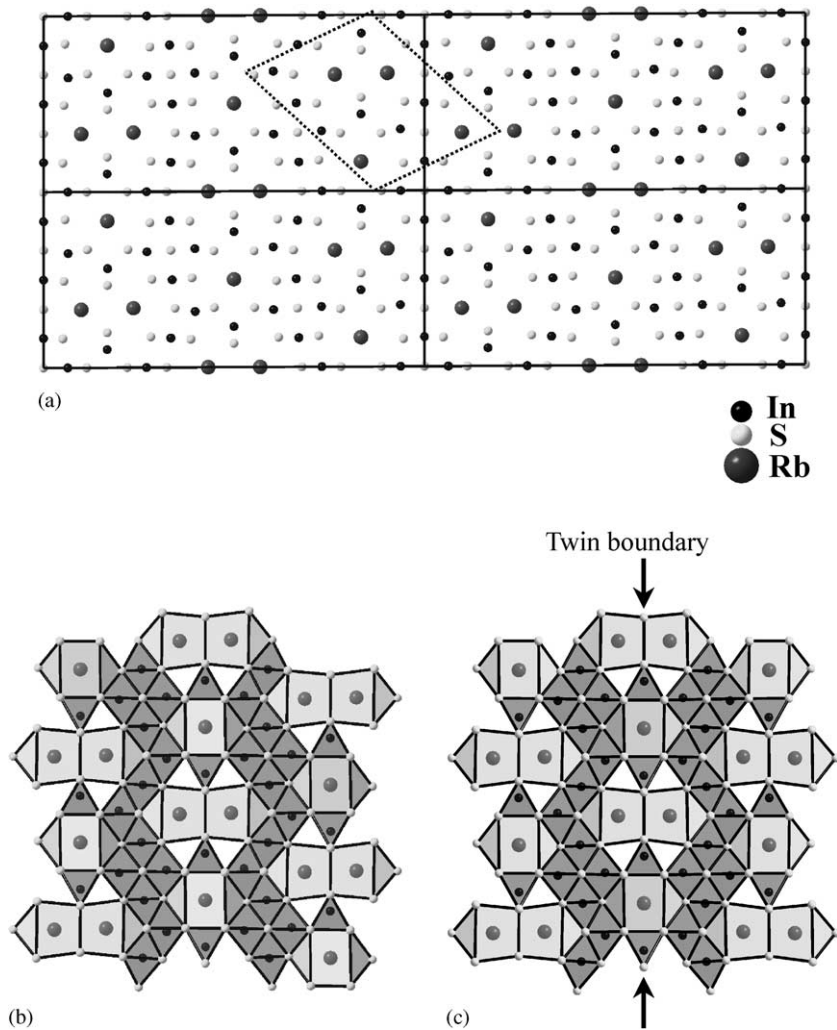
FIG. 4. (a) Transformation of the monoclinic unit cell of RbIn$_3$S$_5$ into larger pseudo- orthorhombic cells (step I, see text). (b) and (c) Section of the ideal structure and of the twinned structure in polyhedral representation (projections along [010]).

$(hkl, h + l \neq 3n)_1$ and $(hkl, h + l \neq 3n)_2$ are separated. The twin index is $i = 3$.

Referring to the monoclinic unit cell of the single domains, the transformation of a zone axis u is defined by the twin matrix T, [for the conventions of matrix multiplication see (15)] as follows:

$$\begin{pmatrix} u' \\ v' \\ w' \end{pmatrix} = T \begin{pmatrix} u \\ v \\ w \end{pmatrix} \quad \text{with } T = \begin{pmatrix} \frac{1}{3} & 0 & \frac{2}{3} \\ 0 & \bar{1} & 0 \\ \frac{\bar{4}}{3} & 0 & \frac{\bar{1}}{3} \end{pmatrix}.$$

Consistent with this geometrical description of the twinning we observed strong irregularities in the contrasts of HREM images of twinned crystallites indicating the presence of domains with different zone axes, e.g., [001] and [$\bar{4}0\bar{1}$].

An essential in the determination of the twin law (16) is the distinction between twofold axes and mirrors acting as twin elements which are aligned in the direction of the twin boundary. In RbIn$_3$S$_5$ the difference in applying both possible twin elements is the inversion of the index v of the zone axis [uvw]. Taking into account that an inversion of v (spacegroup $P2/m$) leads to a identical orientation, it becomes evident that both cases are identical. In the following the twin element is defined to be a mirror perpendicular to [$20\bar{1}$].

A second possible feature of the twinning could be a shift between two differently oriented domains (16). Tilting experiments performed at the twin interface exclude any translational component of the twin element. This is also consistent with the interpretation of the structure at the twin boundary (see below).

A special property of the RbIn$_3$S$_5$ structure is the absence of a low-indexed direction, which is exactly perpendicular to [20$\bar{1}$].[3] Taking into account a rectangular orientation of the twin element and [20$\bar{1}$] ($\alpha = 90°$) it is obvious that twinning by merohedry cannot be exactly fulfilled. Hence, we observed in diffraction patterns of twinned crystallites (see the enlarged sections of diffraction patterns in Fig. 2e) a significant splitting of reflections hkl, $h + l = 3n$ and a variation of the reciprocal distances between pairs of reflections $(hkl, h + l \neq 3n)_1$ and $(hkl, h + l \neq 3n)_2$ (see arrows in Fig. 2e). As indicated in Fig. 3e, simulated patterns of superimposed reciprocal lattices exhibit significant differences even for small variations of α. According to our observations the geometry of all diffraction patterns of twinned crystallites is in good agreement with Fig. 3e, center thus indicating a vertical orientation between [20$\bar{1}$] and the twin element.

Model of the Twinned Structure, Simulation of the Contrasts

In order to simulate HREM images of twinned crystals, a model of the structure was assumed which contains all symmetry elements of the ideal structure and an additional mirror at the twin boundary, as determined from HREM images. The construction of this model consists of three important steps (I–III): (I) Transformation of the ideal structure into a triclinic one, spacegroup $P1$, which contains the symmetry elements of the monoclinic structure as pseudo-symmetry elements. The triclinic structure (index "tr") is obtained applying the matrices $\boldsymbol{P}$ and $\boldsymbol{Q}$ [referring to (15)]:

$$(a_{tr}, \, b_{tr}, \, c_{tr})(= a, \, b, \, c)\boldsymbol{P} \text{ and } \begin{pmatrix} x_{tr} \\ y_{tr} \\ z_{tr} \end{pmatrix} = \boldsymbol{Q} \begin{pmatrix} x \\ y \\ z \end{pmatrix}$$

with

$$\boldsymbol{P} = \begin{pmatrix} 0 & \bar{1} & 2 \\ \bar{1} & 0 & 0 \\ 0 & \bar{1} & \bar{1} \end{pmatrix} \text{ and } \boldsymbol{Q} = \begin{pmatrix} 0 & \frac{\bar{1}}{3} & \frac{1}{3} \\ \bar{1} & 0 & 0 \\ 0 & \frac{2}{3} & \frac{1}{3} \end{pmatrix}.$$

The lattice parameters of the triclinic structure are $a_{tr} = 3.777$ Å, $b_{tr} = 15.622$ Å, $c_{tr} = 33.816$ Å, $\alpha_{tr} = 89.72°$, $\beta_{tr} = 90.00°$, $\gamma_{tr} = 90.00°$. The cell volume is tripled with respect to the original cell. The description of the structure with the triclinic cell leads to nine independent positions for the rubidium, 27 for the indium and 45 for the sulfur atoms. The transformation of the structure is illustrated in Fig. 4a as a projection on $[100]_{tr} = [0\,1\,0]$, the solid lines representing b_{tr} and c_{tr}, the dashed lines a and c of the ideal structure.

[3] The angle $\angle$ ([20$\bar{1}$], [101]) is 89.7°.

In the second step (II) a superimposed structure is formed by applying a mirror exactly perpendicular to $[001]_{tr}$ in the position of the twin boundary. Hence the number of atomic positions is doubled compared to the triclinic structure of step I. In order to describe both parts of the superimposed structure in one common unit cell, the angle α_{tr} was rounded to be exactly 90°. Thus the structure of step II is orthorhombic, the spacegroup is $Pmmm$. Having in mind step III it is a better choice to describe the structure in $P1$, with all symmetry elements of the orthorhombic structure being pseudo-symmetry elements. The simulation of the diffraction pattern of this superimposed structure is in good agreement with experimental ones obtained from twinned crystals with approximately equal parts of both domains within the observed region. For large domains the diffuse scattering is not significant, see below.

In the last, step III, a segregation of the superimposed structure at the twin boundary is applied omitting any superposition of the two twin domains. The twin boundary (see arrows in the polyhedral representation in Fig. 4c) contains the centers of the condensed and single polyhedra, as well as the centers of the InS$_4$ tetrahedra. The comparison with the ideal structure, displayed in Fig. 4b, emphasizes that no distortion of these structural units is necessary to form the twin boundary.

The simulation of the contrasts via the multi-slice formalism was based on the described supercell of model III. Figure 5a displays a series of HREM micrographs with inserted computer simulated images exhibiting excellent agreement. The enlarged section of Fig. 5b (taken near Scherzer defocus, see above) can be interpreted using a projection of the twinned structure (model III). The interpretation of contrasts is the same as in the case of defect-free crystals (see Fig. 2b). Dark spots highlighted by white arrows correspond to the potential of rubidium atoms in the condensed polyhedra (Figs. 5b and 5c). The ellipsoidal marks enclose contrasts corresponding with indium and sulfur atoms forming blocks of InS$_6$ octahedra.

Unified Concept for the Structure Description

In order to characterize the relation between the ideal and the twinned structure, a unified approach can be applied which is also used to illustrate the high compatibility of twinned domains. According to this approach the structure is decomposed into two layers, layer 1 consisting of indium atoms, and layer 2 formed by the polyhedral network depicted in Fig. 6a.

In addition to the symmetry elements of spacegroup $P2/m$, the layers are characterized by special symmetry elements. Layer 2 possesses two additional mirrors aligned perpendicular to [20$\bar{1}$] and [101]. The deviations from this approximate orthorhombic mmm symmetry are minor,
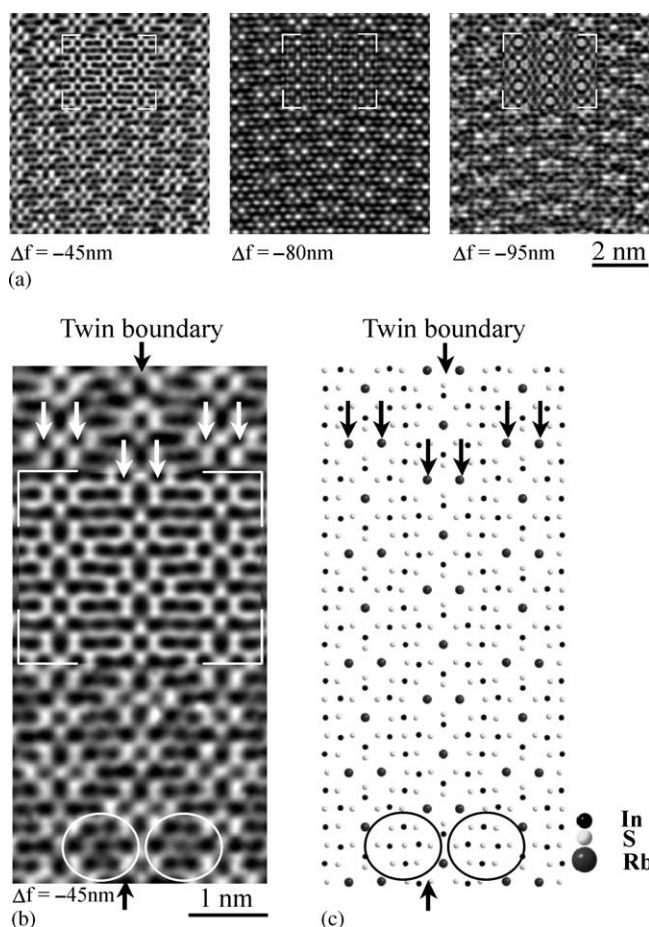
FIG. 5. (a) Series of HREM micrographs of twinned crystals with variable defocus Δf and inserted simulated images (zone axis: [010], thickness: 3.8 nm), (b) HREM image taken near Scherzer defocus, (c) projection of the twinned structure. For markings see text.

structure (third possibility, Fig. 6c), the shifts of $\frac{1}{3}$ along [101] and $\frac{2}{3}$ along [101] are combined. Hence the second layer of type 2 (from the left in Fig. 6c) containing the twin boundary (see arrows) is characterized by a shift of $\frac{1}{3}$ along [101], which is reversed (due to twinning) to $\frac{2}{3}$ along [101] in the third layer. The connection of the differently shifted layers by sulfur atoms is approximately identical to the one in the ideal structure. Hence twinning does not lead to significant structural distortions with respect to the ideal structure.

The differences between real structures characterized by shifting of the above-described layers and twinned structures with a mirror located at the twin boundary are minor. A closer inspection results in small but significant differences of both models. This subject will be discussed in the next section.
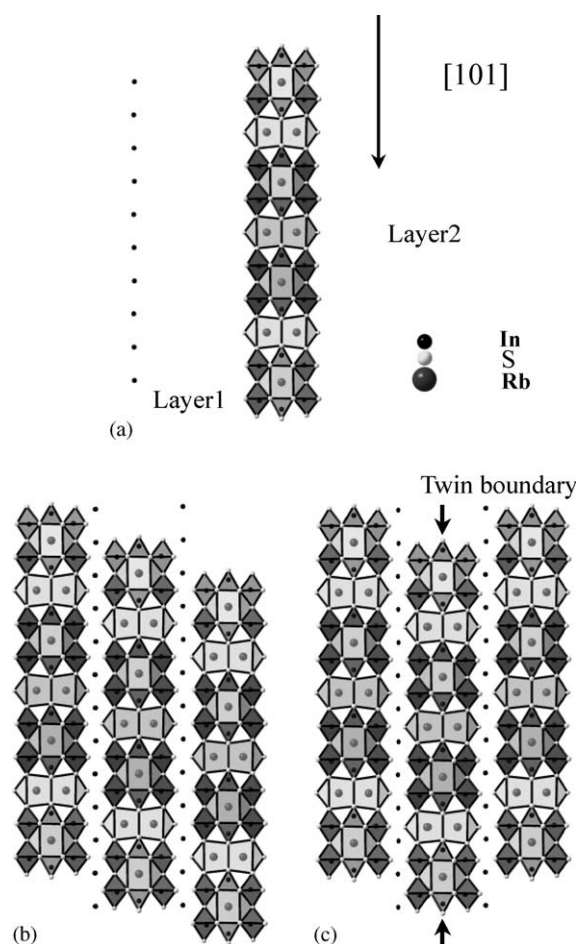

FIG. 6. (a) Layers 1 and 2 viewed edge-on down [010] serving for a unified description of the structure of RbIn$_3$S$_5$. Representation of the ideal structure (b) and the approximated twinned structure (c). For clarity the distance between consecutive layers of type 2 is increased. In reality layers of type 2 are directly linked by sulfur atoms which are drawn twice in (b) and (c).
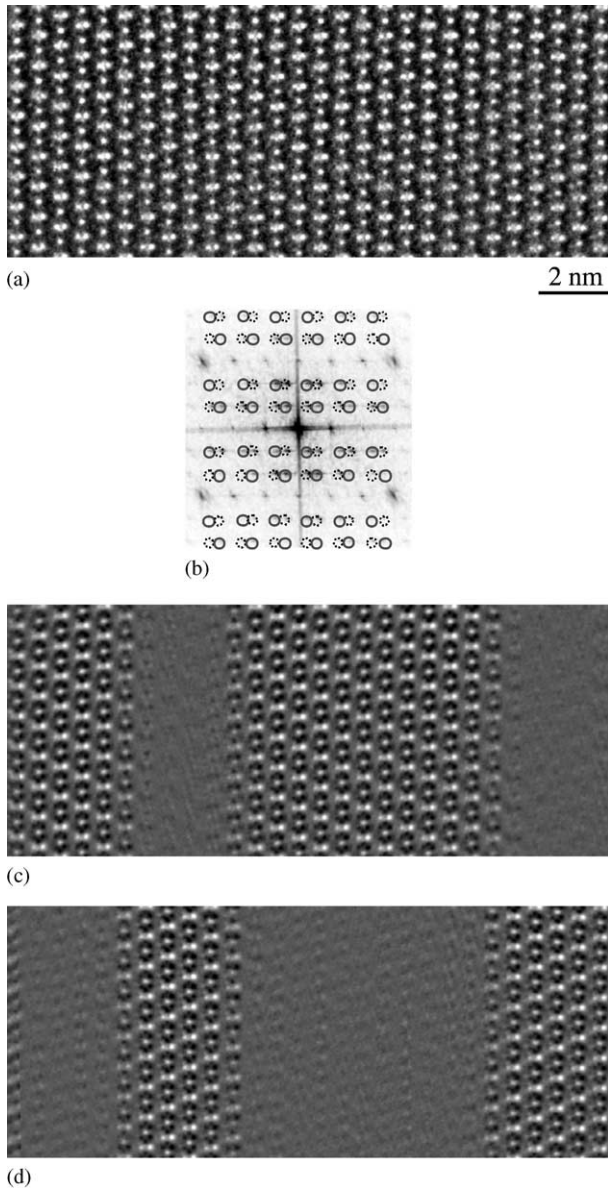
therefore the formation of a twin boundary in the center of layer of type 2 is facilitated. The interlock of the different layers is essential for the understanding of possible variations of the real structures of RbIn$_3$S$_5$. Layer 1 acts as a spacer between successive layers of type 2; the indium atoms of layer 1 center InS$_6$ octahedra between two layers of type 2. These octahedra are repeated by a short translational component of $\frac{1}{3}$ along [101]. With respect to the relative shift of consecutive layers of type 2, three different possibilities are compatible with the translational component of layer 1: 0, $\frac{1}{3}$ along [101] and $\frac{2}{3}$ along [101]. The first possibility (0) involves the direct connection of the condensed polyhedra via common corners. We found no indication for the existence of this first possibility. The second one (Fig. 6b) represents the ideal structure with consecutive layers of type 2 shifted by $\frac{1}{3}$ along [101], or $\frac{2}{3}$ along [101] if the structure is reversed. In the twinned

FIG. 7. Image processing in order to highlight the polysynthetic twinning. (a) unprocessed image (zone axis [010]), (b) FFT of a square region of image (a), circular mask indicated by solid and dashed circles for the two different orientations; (c) and (d) processed images.

Sequence of Twin Lamellas

As a rule the twinning of RbIn₃S₅ is polysynthetic, i.e., it is repeated several times within one crystallite. The twin domains form lamellas with an extension of a few nanometers perpendicular to the twin boundary. A first analysis of the morphology of twinned crystals by light microscopy and SEM (see Introduction) indicates the presence of a large number of irregularly spaced stripes on the surface of the crystals. The stripes are aligned

perpendicular to [010], hence their orientation is identical to that of the twin interfaces. To conclude, it is probable that there is a direct connection between twinning and this special feature of the morphology of RbIn₃S₅ crystals.

In order to visualize the sequence of nanosized domains with alternating orientations, HREM is a suitable method and image processing techniques can be used, see Fig. 7 for [010]. In fast fourier transforms (FFTs), calculated from images of twinned crystals, signals of both orientations can be separated using a suitable mask, see Fig. 7b. Diffuse intensities and all (partially) overlapping reflections (hkl, $h + l = 3n$) are omitted by this procedure. In the next step it is possible to calculate images for both orientations separately, see Figs. 7c and 7d. The resulting images may show artifacts due to the filtering, but they verify the presence of twinned domains with two possible orientations and allow to measure the geometrical details of the twin lamellas easily.

The widths of the alternating twin lamellas are defined by the distance between two consecutive twin boundaries. As a rule, twinned crystals exhibit a random distribution of
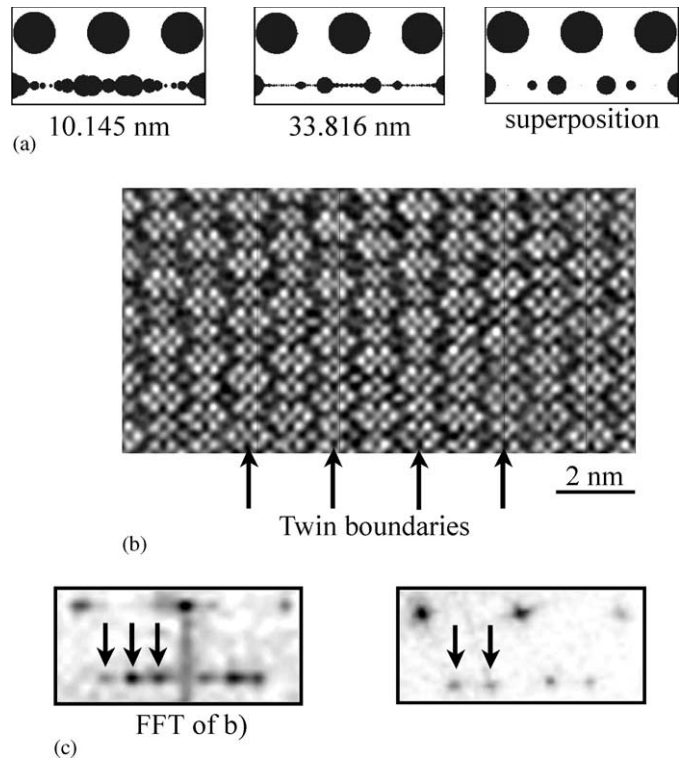

FIG. 8. (a) Sections of simulated diffraction patterns, assuming periodically twinned crystals with increasing width (see specification) of the twin lamellas, zone axis [010]. The pattern designated by "superposition" was calculated on the basis of the superimposed model (see step II). (b) HREM micrograph of a nanosized ordered region, (c) sections of FFTs. Left: FFT of a square region of image (b), right: single twinned crystal. The changes in the periodicity due to the ordering of the twin boundaries are indicated by the arrows.
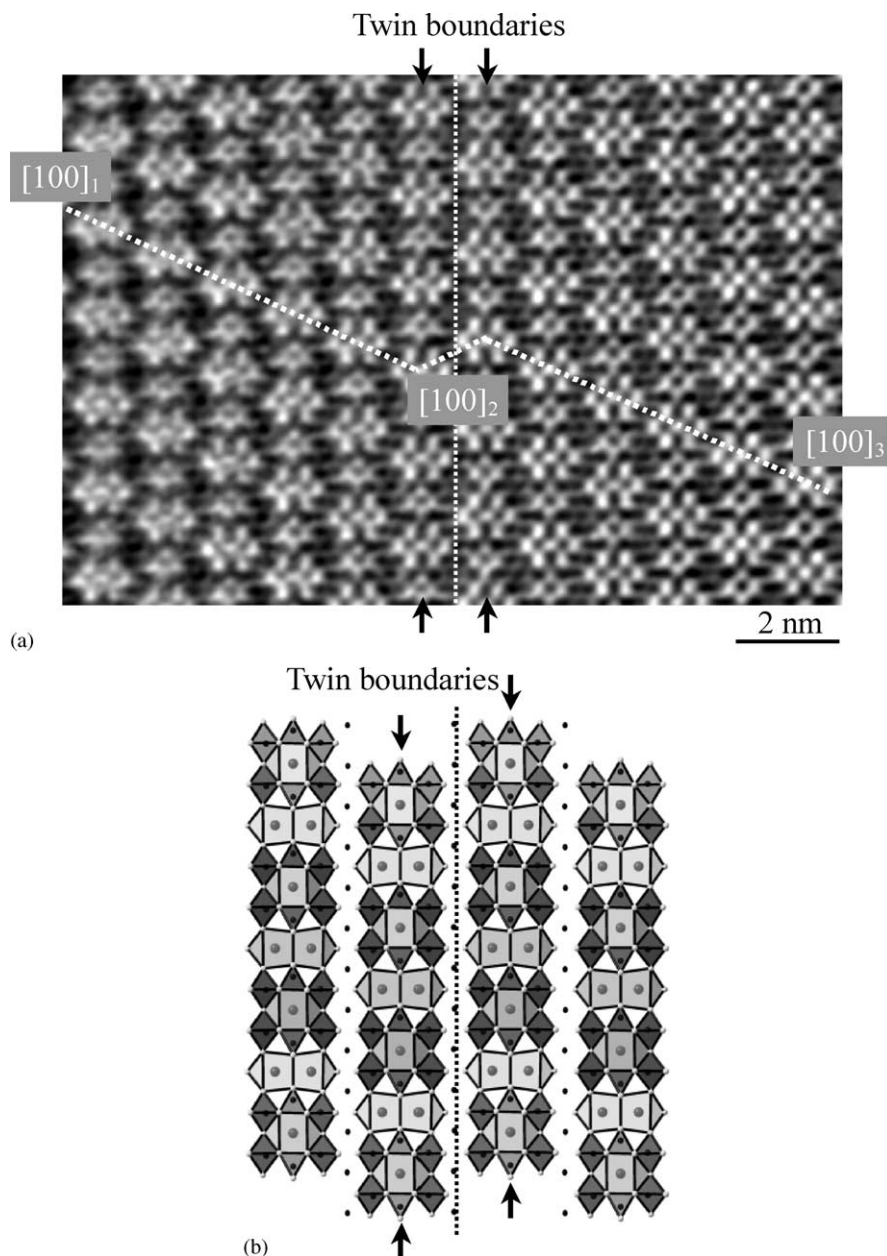
FIG. 9. Back-to-back twinning in RbIn$_3$S$_5$: (a) HREM micrograph, the orientations of domains 1–3 are indicated by their directions [100], dashed line: possibly existing APB; (b) interpretation using the unified structure model (arrows: twin boundaries, dashed line: APB).

their widths. In SAED patterns this leads to the formation of weak diffuse lines between the Bragg reflections (direction of the lines: [$\bar{1}$01]*). A clear relationship between increasing intensities of the diffuse scattering and the density of the twin boundaries is observed.

A random distribution of the widths of twin lamellas does not exclude an equispaced sequence of twin boundaries in small areas of the crystallites. In this case the width of consecutive twin lamellas is identical and these ordered areas establish a locally ordered variation in the structure of RbIn$_3$S$_5$. Consequently, diffraction experiments should

show Bragg reflections indicating the periodicity of the new structure. The width of the twin lamellas exhibits a significant influence on diffraction patterns, as shown in the simulations of Fig. 8a. Each simulation is based on a structure model characterized by a periodic sequence of equispaced twin boundaries with the specified distance between them. For large distances of the twin boundaries, the simulated patterns approximate the diffraction pattern based on the superposition of two twin domains (step II, see above). Therefore, it was expected that especially small domains show significant differences from the superposi-

tion image. As shown in Fig. 8b, these ordered regions are very narrow, and diffraction experiments cannot be performed to examine them separately. The distance of the four equispaced twin boundaries (see arrows) is only 22.6 Å. FFTs are helpful tools for a quick search for nanoscaled ordered regions. The shape and distance of the signals with hkl, $h + l \neq 3n$ (see arrows) change significantly depending on the sequence of the twin lamellas. The diffuse scattering of a random sequence concentrates in Bragg reflections in the case of the ordered regions. Figure 8c, left displays a section of the FFT of a square region of Fig. 8b. The change in the local periodicity of the structure is indicated by the variations of the distances of the signals with hkl, $h + l \neq 3n$ as shown in Fig. 8c left and right.

A special case is met for the minimum possible distance of two twin boundaries ["unit cell level twinning" (17)], i.e., width of the lamella being approximately 11.3 Å. Here the twinning is reversed immediately by a second mirror acting as twin element. The arrows in Fig. 9a mark the twin boundaries which limit the width of domain 2 located in the center of the HREM micrograph to this minimum value. We call this special case of forming a twinned crystal "back-to-back twinning."

Referring to Fig. 9a domain 2 acts as a spacer between the identically orientated domains 1 and 3, see the dashed lines marking [100] for the three domains. A closer inspection of the micrograph gives evidence for an alternative description (18) of this real structure. Taking into account a shift in the center of domain 2, domains 1 and 3 are separated by an antiphase boundary (APB, see vertical dashed line in Fig. 9a) and not by domain 2. SAED patterns recorded on crystals with back-to-back twinning do not differ significantly from the diffraction patterns of ideal crystals. Hence this type of twinning is the only one which cannot be detected easily by diffraction experiments.

The close relationship between back-to-back twinning and shifting at the possibly existing APB is emphasized by the unified structure model discussed above. The arrangement of the structural units, layers 1 and 2, in the case of back-to-back twinning is shown in Fig. 9b. The alternative description of the real structure is characterized by consecutive layers of type 2 shifted by (starting from left in Fig. 9b) $\frac{1}{3}$ along [101], $\frac{2}{3}$ along [101] and $\frac{1}{3}$ along [101]. The simultaneous formation of a possibly existing APB (see dashed line in Fig. 9b) between the two twin boundaries is evident.
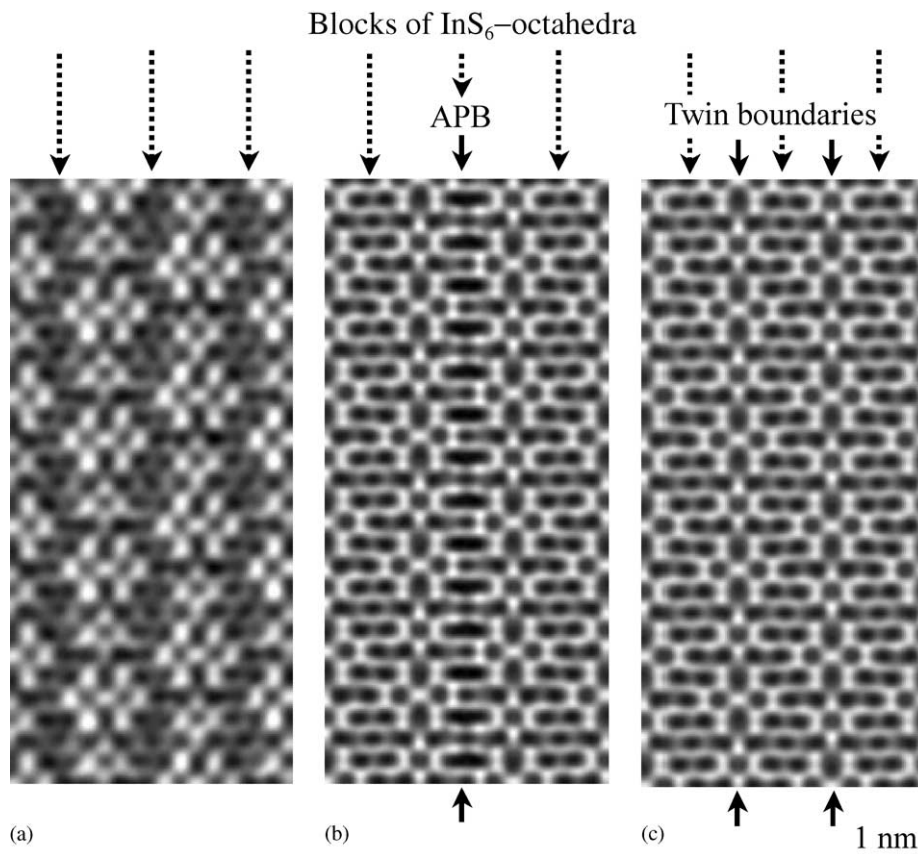

FIG. 10. (a) Experimental HREM image in the case of back-to-back twinning, $\Delta f = -45$ nm. (b) Simulated image based on model 2 (containing an APB, thickness = 1.9 nm). (c) Simulated image based on model 1 (containing two twin boundaries, $t = 1.9$ nm).
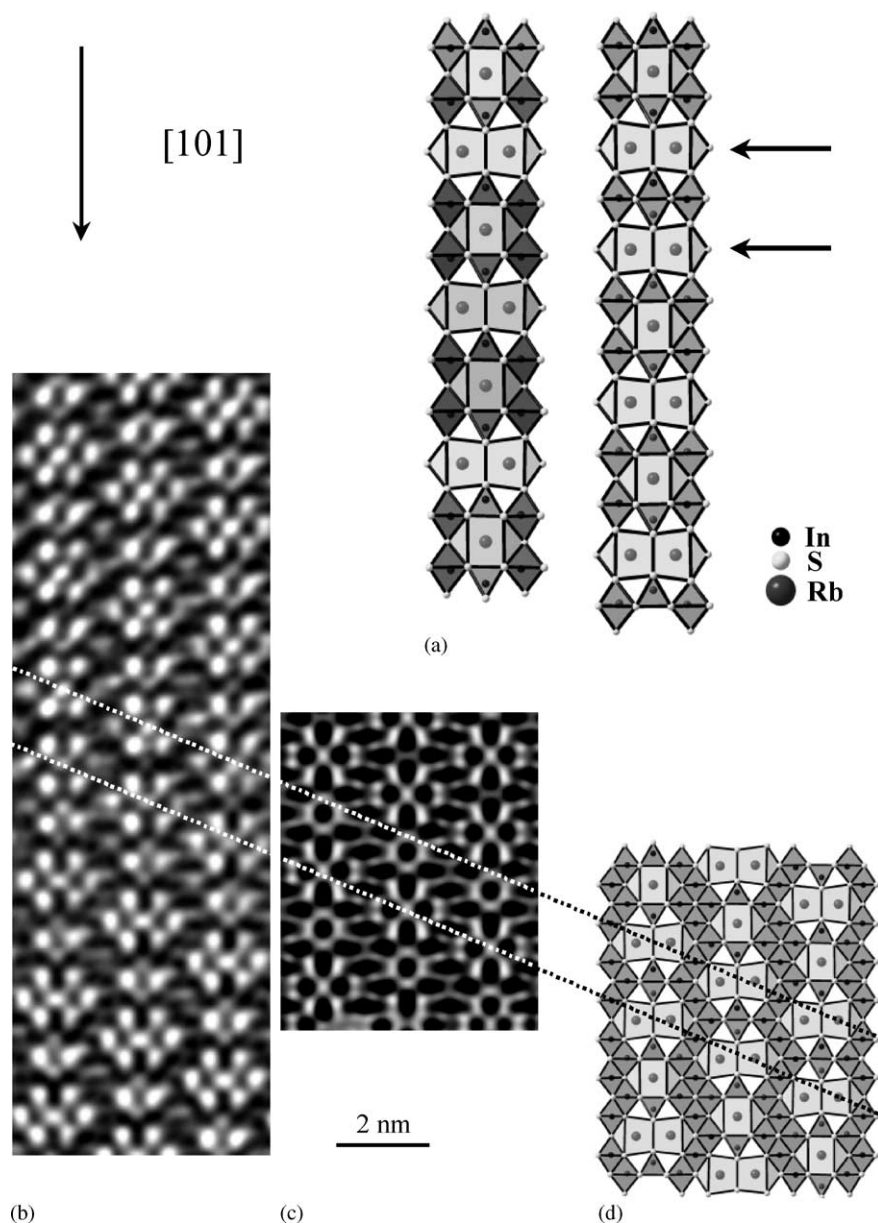
FIG. 11. (a) Variations of layer 2 projected along [010]. Left: periodic ideal structure, right: structure with broken periodicity in [101]. (b) Experimental image ($\Delta f = -50$ nm). (c) Simulated image ($t = 1.9$ nm, zone axis [010]). (d) Projection of the supercell in polyhedral representation (dashed lines parallel to [100]).

In order to distinguish between twinning and shifting, a closer inspection of the structure at the hypothetical APB is important. For the simulation of the contrasts the defects must be described in a suitable supercell. The model of the back-to-back twinning (model 1) starts from the triclinic setting after step 1 (index tr, see above). In a first step c_{tr} is doubled and mirrors are inserted at positions $z = \frac{1}{4}$ and $\frac{5}{12}$ perpendicular to $[001]_{tr}$. The resulting structure is cut at $z = \frac{5}{6}$, and all atomic positions are transformed in order to describe the structure in a new (referring to c smaller) unit cell with the cell parameter $c_{model\,1} = 56.3607$ Å. The starting

point of the APB model (model 2) was again the transformed triclinic structure with doubled c_{tr}. The set of atomic parameters was doubled in the following step introducing a relative shift of $\frac{2}{3}$ along [101] between them. In the last step the atoms of both data sets were separated at the supposed APB, hence introducing a shift of $\frac{2}{3}$ along [101] between the two domains. The compatibility of the two domains at the boundary is not perfect. Taking into account the largest positional deviations, those of the sulfur atoms, the APB was constructed by averaging these positions of both data sets.

These models were the basis for the simulation of HREM images within the multislice formalism. The comparison between experimental and simulated images is displayed in Fig. 10. In the experimental image (Fig. 10a) vertical blocks of contrasts representing InS_6 octahedra are highlighted by dashed arrows. These blocks are identical, consecutive blocks are reversed only. With regard to the location of the boundaries in model 1 (see solid arrows in the simulated image in Fig. 10c), it becomes evident that these blocks are not affected by the twinning (except that they are reversed). In the case of model 2, an APB is located in one of these blocks as indicated by the solid arrows in Fig. 10b. Therefore, slight variations in the contrast of consecutive blocks are identifiable. Referring to this detail, only the simulation of model 1 (Fig. 10c) shows good agreement with the experimental one. Hence, we can conclude that the real structures displayed in Figs. 9a and 10a must be characterized by a back-to-back twinning of $RbIn_3S_5$.

Indications for Other Variations of the Real Structure

The existence of a great diversity of crystal defects obtained in $RbIn_3S_5$ underlines that variations of the real structure are not limited to the above-discussed twinning. The high compatibility of the characteristic structural units enables them to form different real structures by combining these units in the sense of a construction kit. The polyhedral representations in Fig. 11a, left shows the strictly periodic sequence of the polyhedra in layer 2 along [101]. This sequence is realized in the ideal structure and is not affected by the twinning discussed above. Figure 11a, right displays one of the possibilities to break this periodicity forming a modified type of layer 2 (the arrows mark two consecutive condensed polyhedra in Fig. 11a, right). The two condensed polyhedra are linked by two InS_4 tetrahedra which are connected via common edges. A possible connection of these modified layers, i.e., layer 2 with layer 1 can be displayed by the micrograph in Fig. 11b which was taken near Scherzer defocus ($\Delta f = -50$ nm). In analogy to the ideal and the twinned structure the dark spots corresponding to the potential of rubidium atoms in the condensed polyhedra are aligned in [100] (see dashed lines in Fig. 11b–d). Considering the sequence of the contrasts with regard to [101] it is evident that the periodicity is violated. As indicated by the dashed lines in Fig. 11d two pairs of rubidium atoms centering the condensed polyhedra are directly linked together. Thus we can assume the formation of modified layers 2 as shown in Fig. 11a, right. A first simulation of the images based on a suitable supercell (see Fig. 11c) reproduces the sequence of the contrasts. The projection of the supercell (Fig. 11d) indicates that the boundary located in the center of the

dashed lines in Fig. 11b–d is aligned in [100] which is in good agreement with the experimental image.

In contrast to twinned and ideal crystals of $RbIn_3S_5$ with perfect periodicity in the layers, observation for crystals with disturbed periodicity along [101] is affected by radiation damage. Thus the agreement between experimental (Fig. 11b) and simulated images (Fig. 11c) is limited and special experimental methods (e.g., low-dose modes) must be taken into account as future options. A second motive for additional HREM observations is based on the analysis of XRD data in consideration of the twinning. The residual densities (see above) become minor but some of them are still remarkably high. These peaks indicate that further variations in the real structure of $RbIn_3S_5$ could be present which are not linked with the discussed twinning.

REFERENCES

1. W. H. Bloss, F. Pfisterer, M. Schubert, and T. Walter, *Prog. Photovolt.: Res. Appl.* **3,** 3 (1995).
2. J. Marcos-Ruzafa, A. Romano-Rodriguez, J. Alvarez-Garcia, A. Perez-Rodriguez, J. R. Morante, J. Klaer, and R. Scheer, *Inst. Phys. Conf. Ser.* **164,** 247 (1999).
3. D. S. Su, W. Neumann, and M. Giersing, *Thin Solid Films* **361–362,** 218 (2000).
4. A. T. Tham, D. S. Su, W. Neumann, P. Schubert-Bischoff, C. Beilharz, and K.W. Benz, *Cryst. Res. Technol.* **36**(3), 303 (2001).
5. C. Manolikas, R. De Ridder, J. Van Landuyt, and S. Amelinckx, *Phys. Stat. Sol. A* **59**(2), 621 (1980).
6. A. T. Tham, D. S. Su, W. Neumann, P. Schubert-Bischoff, C. Beilharz, and K. W. Benz, *Cryst. Res. Technol.* **35**(6–7), 823 (2000).
7. T. Hanada, A. Yamana, Y. Nakamura, O. Nittono, and T. Wada, *Jpn. J. Appl. Phys. Part 2* **36,** L1494 (1997).
8. L. Kienle and A. Simon, *J. Solid State Chem.* **161,** 385 (2001).
9. C. Reiner, H. J. Deiseroth, M. Schlosser, and L. Kienle, *Z. Anorg. Allg. Chem.* **628,** 249 (2002).
10. H. J. Deiseroth and C. Reiner, *Z. Anorg. Allg. Chem.* **624,** 1839 (1998).
11. H. J. Deiseroth, *Z. Kristallogr.* **117,** 307 (1986).
12. H. J. Deiseroth, C. Reiner, M. Schlosser, and L. Kienle, *Z. Anorg. Allg. Chem.*, accepted for publication.
13. F. Liebau, *Naturwissenschaften.* **49,** 481 (1962).
14. P. A. Stadelmann, *Ultramicroscopy* **21,** 131 (1987).
15. "International Tables for Crystallography," (T. Halm, Ed.), Vol. A. Kluwer Academic Publishers, Dordercht, Boston, London, 1993.
16. R. Ramlau, V. Duppel, A. Simon, S. Cordier, C. Perrin, and M. Sergent, *J. Solid State Chem.* **141,** 140 (1998).
17. S. Andersson and B. G. Hyde, *Solid State Chem.* **9,** 92 (1974).
18. R. Ramlau, *J. Solid State Chem.* **130,** 290 (1997).